

Spontaneous shear flow in confined cellular nematics

G. Duclos^{1,5}, C. Blanch-Mercader^{1,5}, V. Yashunsky^{1,5}, G. Salbreux², J.-F. Joanny^{1,3}, J. Prost^{1,4*} and P. Silberzan^{1,5} ^{1*}

In embryonic development or tumour evolution, cells often migrate collectively within confining tracks defined by their microenvironment^{1,2}. In some of these situations, the displacements within a cell strand are antiparallel³, giving rise to shear flows. However, the mechanisms underlying these spontaneous flows remain poorly understood. Here, we show that an ensemble of spindle-shaped cells plated in a well-defined stripe spontaneously develops a shear flow whose characteristics depend on the width of the stripe. On wide stripes, the cells self-organize in a nematic phase with a director at a well-defined angle with the stripe's direction, and develop a shear flow close to the stripe's edges. However, on stripes narrower than a critical width, the cells perfectly align with the stripe's direction and the net flow vanishes. A hydrodynamic active gel theory provides an understanding of these observations and identifies the transition between the non-flowing phase oriented along the stripe and the tilted phase exhibiting shear flow as a Fréedericksz transition driven by the activity of the cells. This physical theory is grounded in the active nature of the cells and based on symmetries and conservation laws, providing a generic mechanism to interpret in vivo antiparallel cell displacements.

Collective cell migration is classically associated with adhesive cell–cell contacts that can ensure large velocity correlation lengths^{3–12}. However, cells lacking stable cell–cell adhesions such as fibroblasts have been shown to collectively orient in nematic phases^{13–16} and move in ‘streams’ in dense monolayers. Interestingly, such streams have been reported in vivo in embryonic development¹ and cancer². They are often accompanied by bidirectional flows of cells within the same strand. In particular, cancer cells migrating collectively in vivo in effective ‘channels’ formed between collagen fibres have been observed to move away from but also toward the tumour they originate from³. A similar feature has been observed in the migration of neural precursors in development^{17,18}. In vitro, when confined at high density in adhesive tracks, some cell types perfectly align in the main direction of the track and progressively stop moving¹³, while others orient with a finite angle relative to the local direction of the pattern and migrate in streams^{19–21}.

Here, we investigate the orientation and the dynamics of elongated retinal pigment epithelial (RPE1) cells and C2C12 mouse myoblasts within confining stripes and analyse their behaviour within the framework of a hydrodynamic active gel theory.

RPE1 cells in dense monolayers organize together in an active contractile nematic phase (Supplementary Fig. 1). To study their behaviour under confinement, we micropatterned glass substrates

to define adhesive stripes of width L ($10\mu\text{m} < L < 1,400\mu\text{m}$)^{13,22}. In the first 30 h after confluence, cells build a dense monolayer. Between 30 h and 70 h, they also dynamically develop an unstructured second layer on top of the first one, keeping displacements and orientations in register. Therefore, we considered the system as quasi-bidimensional up to 50 h after confluence.

When confined in a 500- μm -wide stripe, RPE1 cells oriented perfectly together within ~ 30 h by annihilation of the characteristic nematic disclination defects^{16,21,23} (Supplementary Fig. 2). Their orientation made a finite angle with the direction of the stripe (Fig. 1a–e). In contrast, NIH-3T3 cells perfectly align with the stripe's direction for widths up to 500 μm (ref. 13; Supplementary Fig. 3A,B,G). Angles were averaged in the direction of the stripe to access the angle profile across its width $\theta(x)$ (Fig. 1f). This tilt angle was larger at the edges ($\theta(x = \pm L/2) = \theta_M = 81^\circ \pm 1^\circ$) and smaller at the centre of the stripe ($\theta(x = 0) = \theta_m = 74^\circ \pm 2^\circ$). Of note, the sign of the orientation (right- or left-handed) of the cells relative to the stripe direction was very reproducible (Supplementary Fig. 4), meaning that this organization reflects an intrinsic tissue-scale chiral symmetry (handedness), as previously reported^{19,24–26}.

The velocity field in the confined cell layer was characterized by large fluctuations. However, averaging in space and time (Fig. 1g) evidenced antiparallel flows of cells along the two edges of the stripe, amounting to a shear flow (Fig. 1h and Supplementary Video 1). We also measured a cell flow in the transverse direction (x) from the edges toward the centre of the stripe (Fig. 1i). The y component of the velocity v_y was significant over a distance $\lambda \approx 40\mu\text{m}$ next to the edges of the stripe and vanished in its centre (Fig. 1j). λ is a friction screening length¹⁶. The x component v_x was of smaller amplitude next to the edges but propagated further in the cell sheet (Fig. 1k). Of note, the shear flows were abolished in the presence of the myosin inhibitor blebbistatin, confirming that they result directly from cell activity. In contrast, blebbistatin did not affect the convergent flows (Supplementary Fig. 5).

We then studied how these different quantities varied with the width of the stripe L ($10\mu\text{m} < L < 1,400\mu\text{m}$; Fig. 2a–g), considering only the fields of view (FOVs) free of topological defects. We found that the angle between the director and the stripe direction increased with width (Fig. 2a–c) and that, after rescaling, the profiles of the convergent flows were universal (Fig. 2g). In contrast, the friction screening length was independent of the stripe width: $\lambda = 44 \pm 10\mu\text{m}$ (Supplementary Fig. 6). This intrinsic screening length prevents a simple rescaling of the v_y shear velocity profiles (Fig. 2e). Strikingly, below a critical width L_c ($40\mu\text{m} < L_c < 50\mu\text{m}$), the cells perfectly aligned with the main direction of the track

¹Laboratoire PhysicoChimie Curie, Institut Curie, PSL Research University - Sorbonne Universités, UPMC - CNRS, Equipe Labellisée Ligue Contre le Cancer, Paris, France. ²The Francis Crick Institute, London, UK. ³ESPCI Paris, Paris, France. ⁴Mechanobiology Institute - National University of Singapore, Singapore, Singapore. ⁵These authors contributed equally: G. Duclos, C. Blanch-Mercader and V. Yashunsky. *e-mail: Jacques.prost@curie.fr; Pascal.silberzan@curie.fr

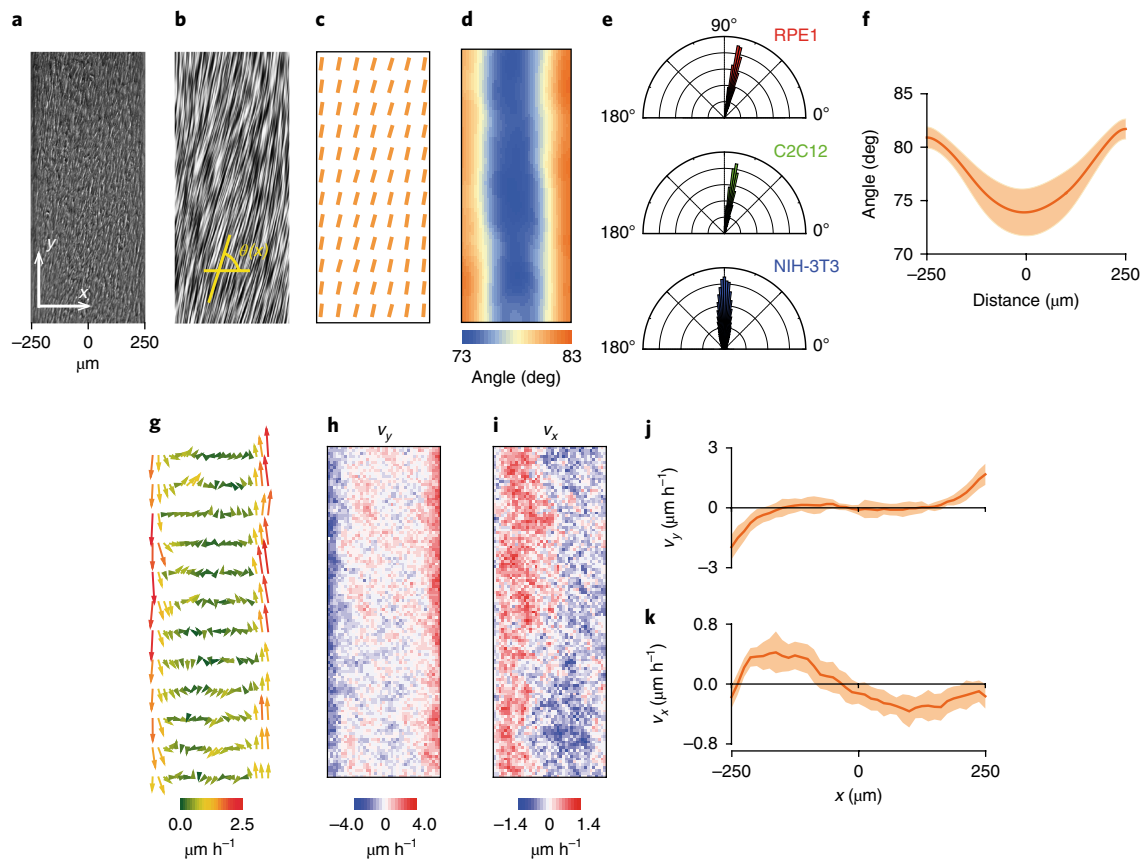


Fig. 1 | Confined RPE1 cells align together with a tilt angle and develop a shear flow. **a–c**, Local angle of the cell bodies when confined in a 500- μm -wide stripe: phase contrast (**a**); line integral convolution (**b**); local director (**c**). Only a small fraction of the directors is displayed for clarity. **d**, Heatmap of the local angle. **e**, Histograms of the angles θ of the cells' bodies (averaged over the width) ($N_{\text{RPE1}} = 38$ FOVs, $N_{\text{C2C12}} = 60$ FOVs, $N_{\text{NIH-3T3}} = 64$ FOVs). **f**, Profile of the orientation angle across the stripe width after averaging along the y direction. **g**, Velocity field within the stripe. The colours code for the speed. Only a fraction of the vectors is displayed for clarity. Note the shear flow (y component) near the edges and the relatively smaller x component of the velocity directed toward the centre. **h, i**, Heatmaps of the y (**h**) and x (**i**) components of the velocity. **j, k**, Profiles of the two components of the velocity across the stripe after averaging over its length (y direction). For all relevant panels, the solid lines are average values and the coloured areas are the standard deviations.

(Figs. 2a and 3a,b,g) and the average shear flow vanished although the cells remained very motile and the convergent flow was not affected (Fig. 3c–f,h,i). The shear velocity fluctuated in space and time about a zero mean (Fig. 3e,i).

In summary, for $L > L_c$, the cell population organizes in a nematic phase with a director at a finite angle with the main direction of the stripe. In parallel, cells spontaneously develop complex flows with shear and transverse components. Below the threshold L_c , cells orient in the direction of the stripe and no net shear flow develops.

To understand these observations, we modelled our system as a confined active nematic fluid^{27,28}. Indeed, despite the obvious practical differences, our confined cells share the same fundamental symmetries as a contractile acto-myosin network powered by ATP hydrolysis between parallel plates²⁹. We therefore developed an adapted version of the physical model of ref.²⁹ that predicts that active nematics confined in a stripe of width L exhibit a generic continuous transition at a critical width L_c between an ordered immobile state and a flowing state. This transition is analogous to the Fréedericksz transition of nematic liquid crystals³⁰ but it is driven by the intrinsic activity of the system rather than an external field. To account for the finite angle of the edge cells (Fig. 2b), we adapted the model by assuming a finite anchoring at the walls. The torque exerted on the cells by the edges is then balanced by the nematic elastic torque (see Supplementary Note).

For widths larger than but close to the critical width ($L \gtrsim L_c$), the angle θ is predicted to vary across the stripe as $\theta(x) \sim \frac{\pi}{2} + \epsilon \sqrt{\frac{L-L_c}{L_c}} \cos(q_c x)$ where $q_c = \frac{2\pi}{L_c}$ and ϵ is a coefficient that depends on the material properties of the system (see Supplementary Note). Similarly, the y component of the velocity is given by $v_y(x) \sim \frac{2Kq_c \epsilon}{\gamma(u+1)} \sqrt{\frac{L-L_c}{L_c}} \sin(q_c x)$, where K is the stiffness associated with splay deformations of the director field, γ is the rotational viscosity and ν is the flow alignment parameter. These quantities are material parameters of the active cells. Therefore, it is expected that the central angle $\theta(0) \sim \pi/2$, the angle $\theta(\pm \frac{L}{2}) \sim \pi/2$ at the edges and the velocity at the edges $v_y(\pm \frac{L}{2})$ all scale as $\sqrt{(L-L_c)}$ (see also Supplementary Note). We note that the large fluctuations of the orientations and velocities (Supplementary Fig. 7) are not described by this mean-field model. For this reason, we focus here only on average quantities.

Fitting model to experiments for $10 \mu\text{m} < L < 150 \mu\text{m}$, we find a very good agreement between these theoretical scaling predictions and the experimental data yielding $L_c = 46 \pm 4 \mu\text{m}$ for RPE1 cells (Fig. 4a,b). Similar results were obtained for C2C12 mouse myoblasts. In this case, we measured $\lambda = 12 \pm 2 \mu\text{m}$ and $L_c = 30 \pm 4 \mu\text{m}$. The theory thus captures the main features of the biological system and in particular the existence of the transition that we now identify as a Fréedericksz transition driven by cell activity. Spontaneous flow transitions are typical of active matter; other examples include low-Reynolds-number turbulence or spontaneous topological singularities in translation and rotation^{27,31}. Here, we demonstrate their

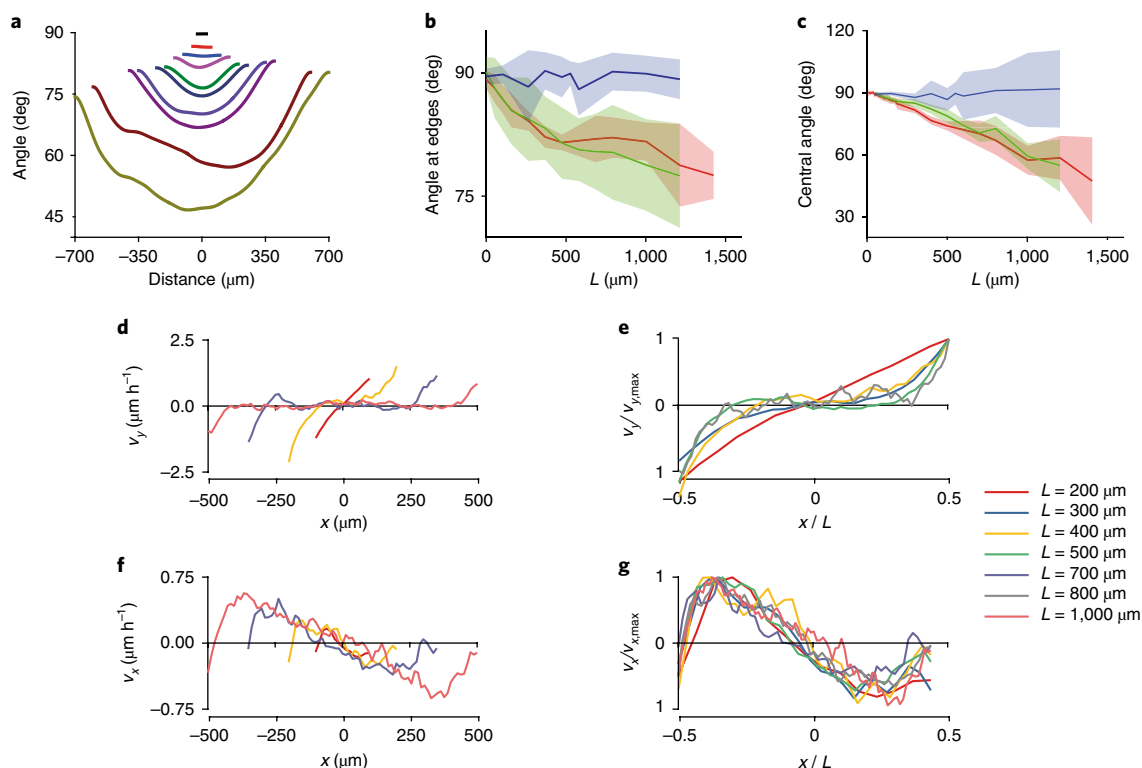


Fig. 2 | Influence of the width of the confining stripe on the behaviour of the cells. **a**, Profiles of the angles across the stripe for different widths L . **b,c**, Evolution of the edge angle (**b**) and the central angle (**c**) of the cell body, as a function of the width. Blue, NIH-3T3 cells; red, RPE1 cells; green, C2C12 cells. The lines are the average values; the coloured areas are the standard deviations. **d**, Profiles of the y component of the velocity for different widths. **e**, Rescaled y component of the velocity as a function of the normalized width. As a result of the friction with the substrate, this scaling does not result in a universal profile. **f**, Profiles of the x component of the velocity for different widths. **g**, Rescaled x component of the velocity as a function of the normalized width. In this case, this scaling results in a universal profile. All experiments were performed with RPE1 cells except when indicated.

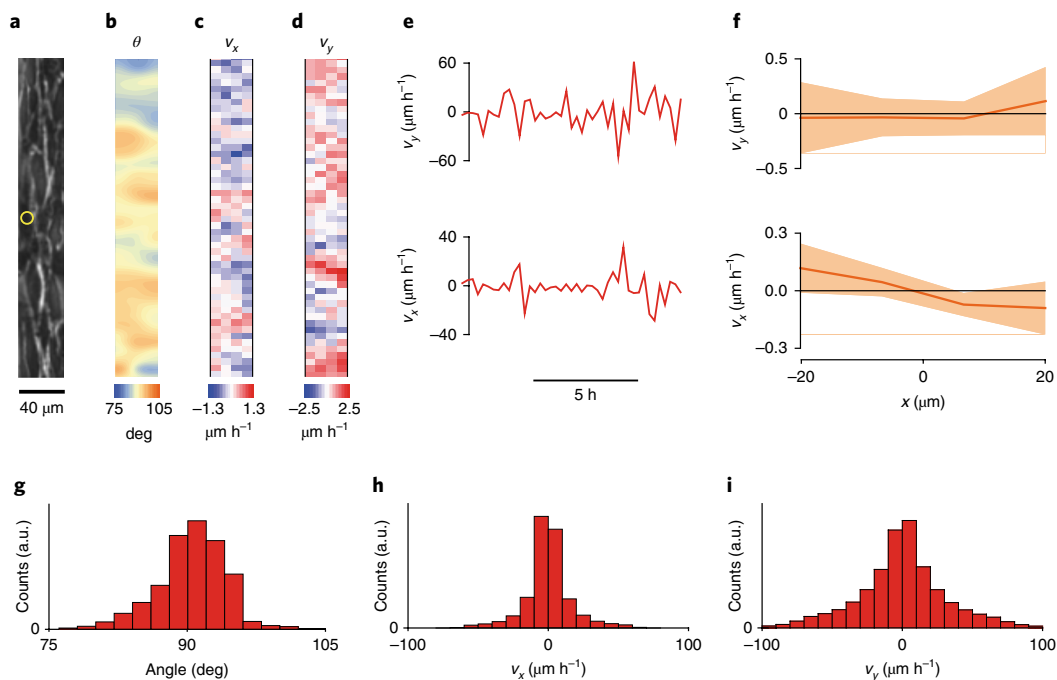


Fig. 3 | Below a critical width, the cells orient along the stripe and do not flow on average. **a**, Phase-contrast image of the RPE1 cells in a 40- μm -wide stripe. **b**, The directions of the cell bodies fluctuate in space about a 90° value. **c,d**, The x and y components of the velocity fluctuate in space about a zero value. **e**, Time traces of the x and y components of the velocity. Measurements were taken at the edge of the stripe (see the yellow circle in **a**). The cells are motile but fluctuate about their mean position with no net displacement. **f**, Profiles of the two components of the velocity across the stripe. Note the absence of shear flow ($v_y = 0$) while the convergent flow is maintained (the solid lines are average values and the coloured areas are the standard deviations; $N = 18$ FOVs). **g-i**, Distributions of the angle, and the x and y components of the velocity. $\theta = 90^\circ \pm 4^\circ$; $v_x = 0 \pm 16 \mu\text{m h}^{-1}$; $v_y = 0 \pm 33 \mu\text{m h}^{-1}$. $N = 20$ independent stripes.

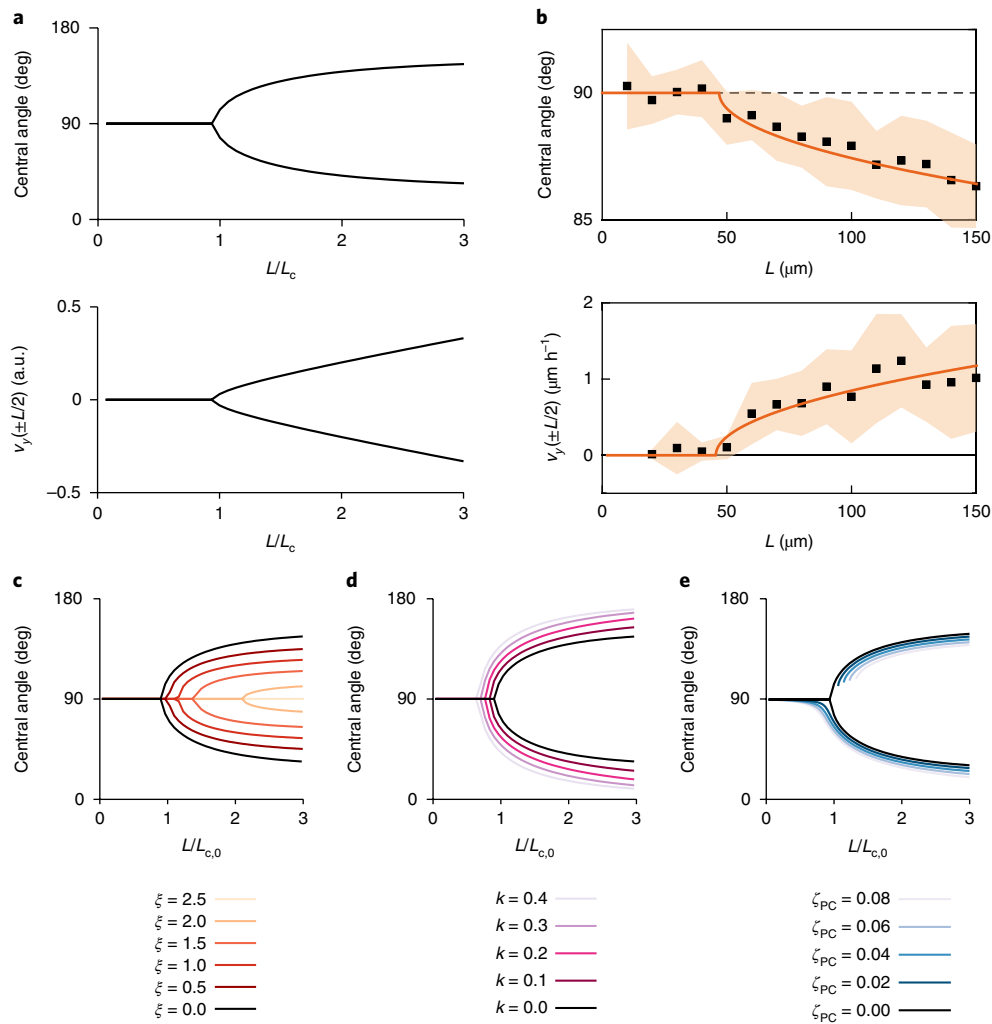


Fig. 4 | Comparison of the experimental results with the active gel theory. **a**, Theoretical prediction of the evolution of the central angle and shear component of the velocity as a function of the width. The width has been rescaled by the critical width. In this initial version of the model, friction, chirality and convergent flows are not considered. **b**, y component of the velocity and central angle as a function of the stripe width. The points are the experimental data (coloured areas are the standard deviations) and the lines are the theoretical fits by a function $\sqrt{L-L_c}$ for $L > L_c$. Note the difference in the horizontal scale compared with that of Fig. 2b,c as we focus here on the close vicinity of the critical width. **c–e**, Impact of the friction (**c**), the transverse flows (**d**) and the chirality (**e**) on the transition. The widths have been rescaled by the critical width. Note the modest impact of transverse flow on the transition and the non-symmetric contribution of the chiral term that selects one branch and smooths out the transition. The parameters have been set to $K = \gamma = -\zeta \Delta\mu = \eta = \frac{v}{2} = W_S = 1$; and $\xi = k = \zeta_{PC} = \lambda_{PC} = 0$ as default values (see Supplementary Note for definitions).

importance in living tissues, which has potentially far-reaching consequences by strongly directing the motion of groups of cells over large distances.

However, some observations for $L > L_c$ could not be described by this simple model. Namely, the $v_y(x)$ profile is screened at a finite length by friction on the surface (Figs. 1h,j and 2d,e and Supplementary Figs. 6 and 8); we observe transversal convergent flows toward the centre of the stripe that are absent in the theory (Figs. 1i,k and 2f,g); and, in the experiments, the system exhibits a net chirality (Supplementary Fig. 4)—that is, the signs of the spontaneous shear flow and tilt angles are well defined and not statistically distributed. These features can be accounted for by recognizing respectively that: momentum is not conserved in our experiments because of the interactions with the substrate; the cell number is not a conserved quantity since cells can divide and extrude; and many biological cellular systems have been reported to be chiral (Supplementary Note).

A finite cell-substrate friction is predicted to impact the velocity profile in the main direction of the stripe, as we observe experimentally on the $v_y(x)$ profile (Supplementary Fig. 8). Large friction coefficients are expected to impair the development of the spontaneous shear flow and the associated tilt (Fig. 4c and Supplementary Fig. 9). As a consequence, the behaviour of the NIH-3T3 cells that fluctuate without generating any net shear flow and align with the stripe direction at all widths¹³ (Figs. 1e and 2b,c and Supplementary Fig. 3) can be explained by either a lower activity of these cells or a larger cell-substrate friction.

The observation of transverse flows from the edges toward the centre of the stripe is associated with a non-vanishing divergence of the velocity that is explained by a non-conservation of the cell number at steady state. The previously observed larger number of cell extrusions in the central part of the confined monolayer compared to its edges²² is the natural explanation for this observed convergent flow (Fig. 4d). We note that the shear flow that originates from cell activity is not coupled to this convergent flow, as blebbistatin-treated

RPE1 cells or untreated NIH-3T3 cells do not exhibit shear flow in spite of proliferation that results in convergent flow (Supplementary Figs. 3J,K and 5C). Of note, in the centre of wide stripes, the shear flow is screened by friction and becomes very small (Fig. 1j and Supplementary Fig. 6), while the convergent flow is not screened (Fig. 1k). We find that the dynamics of the director's orientation is controlled by these convergent flows for stripes larger than typically $1,000\ \mu\text{m}$ (see Supplementary Note, section 2).

On the basis of the left–right symmetry-breaking observed in the experiments (Supplementary Fig. 4), we introduced in the hydrodynamic equations the chiral terms reflecting active mechanical and orientational torques, independently of the spontaneous flow transition^{32,33} (Supplementary Note). This chiral contribution is the only finite term for $L < L_c$ and, as in any symmetry-breaking transition, it selects only one of the two possible shear-flowing states for $L > L_c$, therefore explaining the observed chirality. In fact, the small but finite fraction of experiments showing an opposite chirality confirms that the system is controlled by a mechanical instability. Another consequence of the existence of these chiral terms is to smooth the variation of the velocity with L at $L \sim L_c$ (Fig. 4e). In the present situation, these chiral terms are sufficient to impose the chirality but too small to be experimentally measured from the analysis of the transition.

The coefficients used in the theory to fit the data are of the order of those routinely measured for cell populations (see Supplementary Note), hinting that this framework can be extended to other cell types and situations. Motivated by the in vivo observation of antiparallel flows of cancer cells having detached from the tumour and migrating collectively in confining effective channels³, we confined HT1080 sarcoma cells in adhesive stripes. Indeed, these cells also developed a shear flow very similar to the two cell types studied in the present article, although with an opposite chirality regarding both the tilt angle and the shear flow (Supplementary Fig. 10), highlighting the universality across cell lines of our conclusions.

In light of these in vitro results, we propose that the antiparallel cell displacements that contribute to cell transport in vivo in embryonic development or cancer may be the generic outcome of the confinement of the active nematic gel properties of these cell assemblies.

Methods

Methods, including statements of data availability and any associated accession codes and references, are available at <https://doi.org/10.1038/s41567-018-0099-7>.

Received: 10 August 2017; Accepted: 5 March 2018;

Published online: 16 April 2018

References

- McLennan, R. et al. Multiscale mechanisms of cell migration during development: theory and experiment. *Development* **139**, 2935–2944 (2012).
- Clark, A. G. & Vignjevic, D. M. Modes of cancer cell invasion and the role of the microenvironment. *Curr. Opin. Cell Biol.* **36**, 13–22 (2015).
- Weigel, B., Bakker, G.-J. & Friedl, P. Intravital third harmonic generation microscopy of collective melanoma cell invasion. *IntraVital* **1**, 32–43 (2012).
- Trepat, X. et al. Physical forces during collective cell migration. *Nat. Phys.* **5**, 426–430 (2009).
- Reffay, M. et al. Interplay of RhoA and mechanical forces in collective cell migration driven by leader cells. *Nat. Cell Biol.* **16**, 1–9 (2014).
- Hakim, V. & Silberzan, P. Collective cell migration: a physics perspective. *Rep. Prog. Phys.* **80**, 76601 (2017).
- Petitjean, L. et al. Velocity fields in a collectively migrating epithelium. *Biophys. J.* **98**, 1790–1800 (2010).
- Londono, C. et al. Nonautonomous contact guidance signaling during collective cell migration. *Proc. Natl Acad. Sci. USA* **111**, 1807–1812 (2014).
- Garcia, S. et al. Physics of active jamming during collective cellular motion in a monolayer. *Proc. Natl Acad. Sci. USA* **112**, 15314–15319 (2015).
- Sepúlveda, N. et al. Collective cell motion in an epithelial sheet can be quantitatively described by a stochastic interacting particle model. *PLoS Comput. Biol.* **9**, e1002944 (2013).

- Basan, M., Elgeti, J., Hannezo, E., Rappel, W.-J. & Levine, H. Alignment of cellular motility forces with tissue flow as a mechanism for efficient wound healing. *Proc. Natl Acad. Sci. USA* **110**, 2452–2459 (2013).
- Kabla, A. J. Collective cell migration: leadership, invasion and segregation. *J. R. Soc. Interface* **9**, 3268–3278 (2012).
- Duclos, G., Garcia, S., Yevick, H. G. & Silberzan, P. Perfect nematic order in confined monolayers of spindle-shaped cells. *Soft Matter* **10**, 2346–2353 (2014).
- Elsdale, T. Parallel orientation of fibroblasts in vitro. *Exp. Cell Res.* **51**, 439–450 (1968).
- Kemkem, R., Teichgräber, V., Schrank-Kaufmann, S., Kaufmann, D. & Gruler, H. Nematic order–disorder state transition in a liquid crystal analogue formed by oriented and migrating amoeboid cells. *Eur. Phys. J. E* **110**, 101–110 (2000).
- Duclos, G., Erlenkämper, C., Joanny, J.-F. & Silberzan, P. Topological defects in confined populations of spindle-shaped cells. *Nat. Phys.* **13**, 58–62 (2016).
- Lois, C., Garcia-Verdugo, J. M. & Alvarez-Buylla, A. Chain migration of neuronal precursors. *Science* **271**, 978–981 (1996).
- Nam, S. C. et al. Dynamic features of postnatal subventricular zone cell motility: A two-photon time-lapse study. *J. Comp. Neurol.* **505**, 190–208 (2007).
- Wan, L. Q. et al. Micropatterned mammalian cells exhibit phenotype-specific left–right asymmetry. *Proc. Natl Acad. Sci. USA* **108**, 12295–12300 (2011).
- Raymond, M. J., Ray, P., Kaur, G., Singh, A. V. & Wan, L. Q. Cellular and nuclear alignment analysis for determining epithelial cell chirality. *Ann. Biomed. Eng.* **44**, 1475–1486 (2016).
- Kawaguchi, K., Kageyama, R. & Sano, M. Topological defects control collective dynamics in neural progenitor cell cultures. *Nature* **545**, 327–331 (2017).
- Deforet, M., Hakim, V., Yevick, H. G., Duclos, G. & Silberzan, P. Emergence of collective modes and tri-dimensional structures from epithelial confinement. *Nat. Commun.* **5**, 3747 (2014).
- Saw, T. B. et al. Topological defects in epithelia govern cell death and extrusion. *Nature* **544**, 212–216 (2017).
- Chen, T.-H. et al. Left–right symmetry breaking in tissue morphogenesis via cytoskeletal mechanics. *Circ. Res.* **110**, 551–559 (2012).
- Tee, Y. H. et al. Cellular chirality arising from the self-organization of the actin cytoskeleton. *Nat. Cell Biol.* **17**, 445–457 (2015).
- Xu, J. et al. Polarity reveals intrinsic cell chirality. *Proc. Natl Acad. Sci. USA* **104**, 9296–9300 (2007).
- Marchetti, M. C. et al. Hydrodynamics of soft active matter. *Rev. Mod. Phys.* **85**, 1143–1189 (2013).
- Kruse, K., Joanny, J. F., Jülicher, F., Prost, J. & Sekimoto, K. Generic theory of active polar gels: a paradigm for cytoskeletal dynamics. *Eur. Phys. J. E* **16**, 5–16 (2005).
- Voituriez, R., Joanny, J.-F. & Prost, J. Spontaneous flow transition in active polar gels. *Europhys. Lett.* **70**, 404–410 (2005).
- de Gennes, P.-G. & Prost, J. *The Physics of Liquid Crystals* 2nd edn (Oxford Univ. Press, Oxford, 2003).
- Prost, J., Jülicher, F. & Joanny, J.-F. Active gel physics. *Nat. Phys.* **11**, 111–117 (2015).
- Fürthauer, S., Stempel, M., Grill, S. W. & Jülicher, F. Active chiral fluids. *Eur. Phys. J. E* **35**, 89 (2012).
- Fürthauer, S., Stempel, M., Grill, S. W. & Jülicher, F. Active chiral processes in thin films. *Phys. Rev. Lett.* **110**, 048103 (2013).

Acknowledgements

We thank the members of the Biology-inspired Physics at MesoScales (BiPMS) group and, in particular, F. Ascione, T. Sarkar and H. G. Yevick. We also thank L. Valon for suggesting the use of RPE1 cells. V.Y. gratefully acknowledges the CelTisPhyBio Labex and the EU PRESTIGE programme for financial support. G.S. is supported by the Francis Crick Institute, which receives its core funding from Cancer Research UK (FC001317), the UK Medical Research Council (FC001317) and the Wellcome Trust (FC001317). The BiPMS group and the Physical Approach of Biological Problems group are members of the CelTisPhyBio Labex. The BiPMS group is a member of the Institut Pierre-Gilles de Gennes.

Author contributions

G.D. and P.S. designed the research. G.D. and V.Y. performed the experiments and C.B.-M. and G.S. developed the theory. P.S., J.P. and J.-F.J. supervised the research. All authors analysed the data and participated in writing the manuscript.

Competing interests

The authors declare no competing interests.

Additional information

Supplementary information is available for this paper at <https://doi.org/10.1038/s41567-018-0099-7>.

Reprints and permissions information is available at www.nature.com/reprints.

Correspondence and requests for materials should be addressed to J.P. or P.S.

Publisher's note: Springer Nature remains neutral with regard to jurisdictional claims in published maps and institutional affiliations.

Methods

Cell culture. RPE1 cells (gift from M. Dahan, Institut Curie, France), C2C12 myoblasts (gift from C. Théry, Institut Curie, France), HT1080 cells (gift from P. Chavrier, Institut Curie, France) and NIH-3T3 fibroblasts (gift from K. Laud-Duval, Institut Curie, France) were cultured in Dulbecco's modified Eagle's medium (high glucose + GlutaMAX, Gibco) supplemented with 10% FBS (Sigma) and 1% antibiotics solution (penicillin (10,000 units ml⁻¹) + streptomycin (10 mg ml⁻¹); Gibco) at 37°C, 5% CO₂ and 90% humidity. Blebbistatin (Sigma) was used at a concentration of 3 µM (higher concentrations destroyed the nematic order altogether).

Time-lapse microscopy. Time-lapse multi-field experiments were performed in phase contrast on an automated inverted microscope (Olympus IX71) equipped with thermal and CO₂ regulation. A typical field of view (FOV) was 1.5 mm × 1.5 mm. The displacements of the sample and the acquisitions with a CCD (charge-coupled device) camera (Retiga 4000 R, QImaging) were controlled by Metamorph (Universal Imaging) software. The typical delay between two successive images of the same field was set to 15 or 30 min.

Image processing. Most of the image processing was performed using the ImageJ public domain software. The orientation field was obtained by computing the local structure tensor with the ImageJ plugin OrientationJ^{34,35}. For representation purposes, we occasionally used a line integral convolution under Matlab (MathWorks). The velocity field was mapped by particle image velocimetry (PIV) analysis. Stacks of images were analysed with a custom-made PIV algorithm based on the MatPIV software package for Matlab (MathWorks)⁷. The window size was set to 32 pixels = 23.75 µm with a 0.5 overlap for $L > 30$ µm and 16 pixels = 11.9 µm with a 0.5 overlap for $L = 20$ µm and $L = 30$ µm. The friction screening length λ was measured by fitting two decreasing exponential curves to the v_x velocity profiles.

Micropatterning technique. Clean glass substrates were first uniformly coated with a cell-repellent layer (interpenetrated gel of acrylamide and polyethylene glycol)²². A photoresist mask was then structured directly on top of the layer by classical photolithography methods and air plasma was used to locally etch the protein-repellent coating through this mask. The photoresist was then removed with acetone, yielding a cell-repellent substrate where domains on which cells can adhere (bare glass) have been defined^{22,36}. Owing to the frequent presence of topological defects at widths larger than 1,500 µm, we limited our study to stripe widths between 10 µm and 1,400 µm.

Statistical analysis. Statistical analysis was performed with Matlab (MathWorks) or Origin (OriginLab). Experiments were performed in at least 2 replicas, each using 6-well plates with stripes of two distinct widths per well (for $L = 50$ µm, 100 µm and 200 µm to 1,200 µm) or five distinct widths (for $L = 10$ to 200 µm). The number of analysed FOVs for each width is reported in the list below. Error bars represent the standard deviations over all of the FOVs analysed (pooling all experiments in a single set). FOVs presenting topological defects were excluded from the analysis.

The orientational profiles are all acquired 50 h after confluence. The velocity profiles obtained from the PIV velocity maps are averaged over time ($0 < t < 50$ h post-confluence). Both profiles were averaged along the direction of the stripe.

The widths L analysed in the present study and the corresponding number N of FOVs used for the PIV analysis of RPE1 cells are as follows: (L (µm), N) = (20, 18); (30, 21); (40, 20); (50, 56); (60, 21); (70, 20); (80, 29); (90, 29); (100, 61); (110, 29); (120, 29); (130, 26); (140, 26); (150, 26); (160, 26); (170, 35); (180, 35); (190, 35); (200, 60); (300, 20); (400, 13); (500, 13); (700, 14); (800, 11); (1,000, 18); (1,200, 7).

The widths L analysed in the present study and the corresponding number N of FOVs used for measuring the orientation profiles of RPE1 cells are as follows: (L (µm), N) = (10, 13); (20, 18); (30, 21); (40, 20); (50, 60); (60, 21); (70, 19); (80, 28); (90, 29); (100, 84); (110, 29); (120, 29); (130, 26); (140, 26); (150, 26); (160, 26); (170, 35); (180, 35); (190, 35); (200, 75); (300, 28); (400, 51); (500, 38); (700, 17); (800, 27); (1,200, 24); (1,400, 14).

The widths L analysed in the present study and the corresponding number N of FOVs used for measuring the orientation profiles of C2C12 cells are as follows: (L (µm), N) = (50, 53); (100, 52); (200, 80); (300, 69); (400, 88); (500, 60); (600, 64); (700, 39); (800, 23); (1,000, 29); (1,200, 36).

The widths L analysed in the present study and the corresponding number N of FOVs used for the PIV analysis and estimation of Fréedericksz transition in C2C12 cells are as follows: (L (µm), N) = (16, 6); (32, 10); (40, 11); (50, 16); (65, 8); (80, 9); (95, 6); (140, 10).

The widths L analysed in the present study and the corresponding number N of FOVs used for measuring the orientation profiles of NIH-3T3 cells are as follows: (L (µm), N) = (50, 125); (150, 100); (300, 5); (400, 67); (500, 64); (550, 44); (600, 84); (800, 96); (1,000, 82); (1,200, 98).

Middle angle distribution measurement and PIV analysis of HT1080 cells were obtained from 28 stripes of 125 ± 5 µm width in the course of 25 h, starting from confluency.

Blebbistatin treatment of RPE1 cells was performed 12 h after the cells became confluent on 300-µm-wide stripes. PIV analysis was performed on 9 FOVs for 12 h before and after the blebbistatin treatment.

Life Science Reporting Summary. Further information on experimental design is available in the Life Sciences Reporting Summary.

Data availability. The data that support the findings of this study are available from the corresponding author upon reasonable request.

References

34. Rezakhanlou, R. et al. Experimental investigation of collagen waviness and orientation in the arterial adventitia using confocal laser scanning microscopy. *Biomech. Model. Mechanobiol.* **11**, 461–473 (2012).
35. Rasband, W. S. ImageJv1.46b (US National Institutes of Health, Bethesda, Maryland, 1997–2012).
36. Duclos, G. et al. in *Cell Migration: Methods and Protocols, Methods in Molecular Biology* (ed. Gautreau, A.) **1749**, 387–399 (Humana Press, New York, 2018).

Life Sciences Reporting Summary

Nature Research wishes to improve the reproducibility of the work that we publish. This form is intended for publication with all accepted life science papers and provides structure for consistency and transparency in reporting. Every life science submission will use this form; some list items might not apply to an individual manuscript, but all fields must be completed for clarity.

For further information on the points included in this form, see [Reporting Life Sciences Research](#). For further information on Nature Research policies, including our [data availability policy](#), see [Authors & Referees](#) and the [Editorial Policy Checklist](#).

► Experimental design

1. Sample size

Describe how sample size was determined.

Experiments were performed in at least 2 replicas, each using 6 well plates with stripes of two distinct widths per well (for $L=50\mu\text{m}$, $100\mu\text{m}$ and $200\mu\text{m}$ to $1200\mu\text{m}$) or five distinct widths (for $L=10$ to $200\mu\text{m}$). The exact number of FOV analysed is reported in the paper. The sample size was determined by pooling all the FOV analysed per condition.

2. Data exclusions

Describe any data exclusions.

The stripes with topological defects in the orientation field were excluded from the analysis. Details are provided in the manuscript

3. Replication

Describe whether the experimental findings were reliably reproduced.

The replication failed only if the micropattern are not realized correctly. Otherwise, as long as the cells are confined and do not escape the tracks, all replications were successful.

4. Randomization

Describe how samples/organisms/participants were allocated into experimental groups.

n/a

5. Blinding

Describe whether the investigators were blinded to group allocation during data collection and/or analysis.

n/a

Note: all studies involving animals and/or human research participants must disclose whether blinding and randomization were used.

6. Statistical parameters

For all figures and tables that use statistical methods, confirm that the following items are present in relevant figure legends (or in the Methods section if additional space is needed).

- | | |
|-------------------------------------|---|
| n/a | Confirmed |
| <input type="checkbox"/> | <input checked="" type="checkbox"/> The <u>exact sample size</u> (n) for each experimental group/condition, given as a discrete number and unit of measurement (animals, litters, cultures, etc.) |
| <input type="checkbox"/> | <input checked="" type="checkbox"/> A description of how samples were collected, noting whether measurements were taken from distinct samples or whether the same sample was measured repeatedly |
| <input type="checkbox"/> | <input checked="" type="checkbox"/> A statement indicating how many times each experiment was replicated |
| <input checked="" type="checkbox"/> | <input type="checkbox"/> The statistical test(s) used and whether they are one- or two-sided (note: only common tests should be described solely by name; more complex techniques should be described in the Methods section) |
| <input checked="" type="checkbox"/> | <input type="checkbox"/> A description of any assumptions or corrections, such as an adjustment for multiple comparisons |
| <input checked="" type="checkbox"/> | <input type="checkbox"/> The test results (e.g. P values) given as exact values whenever possible and with confidence intervals noted |
| <input type="checkbox"/> | <input checked="" type="checkbox"/> A clear description of statistics including <u>central tendency</u> (e.g. median, mean) and <u>variation</u> (e.g. standard deviation, interquartile range) |
| <input type="checkbox"/> | <input checked="" type="checkbox"/> Clearly defined error bars |

See the web collection on [statistics for biologists](#) for further resources and guidance.

► Software

Policy information about [availability of computer code](#)

7. Software

Describe the software used to analyze the data in this study.

ImageJ, Matlab, Origin

For manuscripts utilizing custom algorithms or software that are central to the paper but not yet described in the published literature, software must be made available to editors and reviewers upon request. We strongly encourage code deposition in a community repository (e.g. GitHub). *Nature Methods* [guidance for providing algorithms and software for publication](#) provides further information on this topic.

► Materials and reagents

Policy information about [availability of materials](#)

8. Materials availability

Indicate whether there are restrictions on availability of unique materials or if these materials are only available for distribution by a for-profit company.

No restrictions

9. Antibodies

Describe the antibodies used and how they were validated for use in the system under study (i.e. assay and species).

No antibodies were used

10. Eukaryotic cell lines

a. State the source of each eukaryotic cell line used.

RPE-1 cells, source: Dr Maxime Dahan, Institut Curie, UMR 168 Paris France
C2C12 cells, source: Dr Clotilde Théry, Institut Curie
NIH-3T3 cells, source: Dr Karine Laud-Duval, Institut Curie
HT1080 cells, source: Dr Philippe Chavrier, Institut Curie

b. Describe the method of cell line authentication used.

No cell line authentication was performed

c. Report whether the cell lines were tested for mycoplasma contamination.

The cells lines were tested for mycoplasma contamination, results were negative

d. If any of the cell lines used are listed in the database of commonly misidentified cell lines maintained by [ICLAC](#), provide a scientific rationale for their use.

We did not use any commonly misidentified cell lines.

► Animals and human research participants

Policy information about [studies involving animals](#); when reporting animal research, follow the [ARRIVE guidelines](#)

11. Description of research animals

Provide details on animals and/or animal-derived materials used in the study.

No research animals

Policy information about [studies involving human research participants](#)

12. Description of human research participants

Describe the covariate-relevant population characteristics of the human research participants.

no human research participants